VOLCANICA Article in Press

This is an uncorrected proof, meaning that this manuscript has not been copyedited or formatted according to Volcanica's styles and standards. In turn, this means that article content, including text, may still change prior to final publication. Although articles in press do not have all bibliographic details available yet, they can be cited using the year of online publication and the DOI, as follows: author(s)(year), article title, Volcanica, DOI.

Biren, J., Gazel, E. and Lisa, K. (2026) "Analytical set-up for measuring the Infrared Spectral Emissivity of Materials at High Temperature and Microscale", Volcanica, 9(2). doi: 10.30909/vol/mqgi6947.

article in press

Analytical set-up for measuring the Infrared Spectral Emissivity of Materials at High Temperature and Microscale.

Jonas Biren[a,b*], Esteban Gazel[c*], Lisa Kaltenegger[a,b],

[a]Carl Sagan Institute, Ithaca NY, 14853, United States
[b]Cornell University, Department of Astronomy, Ithaca NY, 14853, United States
[c]Cornell University, Department of Earth and Atmospheric Sciences, Ithaca NY, 14853, United States

[*]Corresponding authors:
Jonas Biren and Esteban Gazel
Email address: jonas.biren@cornell.edu , egazel@cornell.edu
*Postal addres*s: Space Sciences Building, Ithaca, NY 14853, United States
ORCiD (JB): 0000-0002-9995-7552
ORCiD (EG): 0000-0002-6385-7672
ORCiD (LK): 0000-0002-0436-1802

Keywords
Emissivity / High-Temperature / Infrared Spectroscopy / Melts / Microscopy

Abstract
Knowledge of how radiative properties vary with temperature in natural and synthetic materials at the microscale is essential for both research and high-temperature industrial applications. During volcanic eruptions, lava temperatures are commonly retrieved using ground- or satellite-based infrared radiance measurements, a technique also applied to volcanic materials across the Solar System and beyond. However, current spectral libraries lack high-temperature, microscale radiative data, partly because emission experiments are technically complex and typically average out small-scale phase heterogeneities. To address this gap, we developed a new analytical set-up capable of measuring in situ radiative properties of homogeneous and heterogeneous opaque material samples at 673–1773 K over a wide spectral range (3–15 μm / 3333–666 cm^{-1}) under a microscope. We present a calibration procedure and methodology to retrieve accurate temperatures for both the sample

article in press

and blackbody reference, enabling improved remote-sensing calibration for terrestrial and extraterrestrial applications.

Second-language abstract

Understanding how hot materials emit infrared radiation is essential for studying volcanoes on Earth and other planetary bodies. Lava temperature is commonly estimated from infrared light measured by ground-based instruments or satellites, but existing reference datasets remain incomplete because they do not capture the behavior of natural materials at very high temperatures or at very small spatial scales. In addition, standard laboratory methods often average out small-scale variations within heterogeneous samples. To address this limitation, we developed a new laboratory setup capable of heating material samples up to about 1773 K while measuring their infrared emission over a broad wavelength range. The system is designed to operate under a microscope and can analyze both homogeneous and heterogeneous materials, as found in natural volcanic rocks. This approach enables more accurate temperature determination and provides data that can improve the calibration and interpretation of remote sensing observations on Earth and in planetary exploration.

article in press

1 Introduction

Currently our knowledge of how efficiently radiative heat is emitted from natural and synthetic silicate-rich materials at high temperatures and in their molten state is limited (e.g., Watanabe et al. 2014; Howell et al. 2020; Giulietti et al. 2025). Thermal radiation heat transfer is of great importance in volcanology for lava flow propagation modeling (e.g., Rogic et al. 2019; Thompson and Ramsey 2021; Li et al. 2021; Biren et al. 2022), heat transport using remote sensing techniques (e.g., Glaze et al. 1989; Lombardo and Buongiorno 2006; Thompson and Ramsey 2020; Nádudvari et al. 2020), and planetary exploration in the Solar System and beyond (e.g., Fortin et al. 2024; First et al. 2024; Paragas et al. 2025; Thompson et al. 2025). However, without constraints of the radiative properties, the retrieval of remote sensing is challenging, compromising their interpretation (Thompson and Ramsey 2021; Biren et al. 2022; Krapez 2025; Giulietti et al. 2025). Nanoscale crystalline phases are an under-investigated component of erupting magmas, yet they may exert primary control on the eruptive style of silicic systems. Laboratory experiments capable of probing the radiative properties of these phases are therefore critical for the interpretation of remote sensing observations of active eruptions. For example, Cáceres et al. (2020) and Di Genova et al. (2020) demonstrated that magmas with identical bulk compositions can produce markedly different infrared spectral signatures due to variations in nanolite populations and degassing histories. Natural or synthesized materials (e.g., natural rocks such as meteorites, coated glasses with micrometric multi layers, crystal-rich samples; Shan et al. 2020; Koirala 2023) used for these applications are increasingly more complex and thus are often limited in size, and therefore the use of a microscopic approach is required for their proper characterization (e.g., observation of local phase change or micron scale damage (see Eckes et al. 2013; Shan et al. 2020; Hardgrove and Rogers 2013). Recent efforts aim to understand the relationship of the radiative properties either at high temperature or at the microscale (e.g., Edwards and Christensen 2013; Wang et al. 2014; Thompson et al. 2021; Rogic et al. 2022; Yao et al. 2022). However, to characterize the intricate processes responsible for changes in the radiative properties of

article in press

heterogeneous samples under varying physical conditions, it is critical to measure the radiative spectra of heterogeneous samples both with micrometer resolution and high temperature. Consequently, inferring the state of material surfaces heavily rely on *in situ* techniques combining microscopy and high temperature capabilities.

As a first approach, one can easily find the radiative properties of rocky materials in available spectral libraries (e.g., RELAB, BED, JPL/Caltech; Salisbury and D'Aria 1992; Pieters and Hiroi 2004; Baldridge et al. 2009; Maturilli and Helbert 2014; Kokaly et al. 2017; Meerdink et al. 2019). However, most of the data found in these libraries were measured at room temperature, and only a few provide microscale measurements that resolve the microstructure and intrinsic heterogeneity of natural samples, thus not reflecting the array of radiative properties at high temperature and microscale resolution needed to answer the specific goals of volcanology and space exploration applications. Laboratory data at high temperatures are scarce, mainly because these measurements are challenging. As Ren et al. (2016) point out, high-temperature emissivity measurements are difficult above ~1273 K because of sample heating, temperature gradients across the measured area, and the need to know the true surface temperature. In addition, every part of the instrument and its surroundings emits thermal radiation, so the measured signal contains a background that is not easy to isolate, and this problem depends strongly on the setup (Xiao et al., 2020). To improve data interpretation, a library of the radiative properties (spectral emissivity and reflectivity) of glassy/molten microscopic surfaces for a wide temperature range is critical.

CEMHTI laboratory (Orleans, France) developed a contactless method capable of measuring the thermal emission of semi-transparent materials up to 2500 K using a laser as heating source for a wide spectral range spanning 0.5–500 μm with two Fourier-Transform Infrared (FTIR) spectrometers (De Sousa Meneses et al. 2015; Biren et al. 2022). Li et al. (2021) and Biren et al. (2022) were the first to demonstrate its applicability to magmatic materials such as glassy and natural phonolite and basalts and Eckes et al. (2013); Brun et al. (2013) for industrial processes. The Planetary Emissivity

article in press

Laboratory at DLR (Berlin, Germany) developed a highly versatile technique capable of measurement the thermal emission of planetary analogs between 0.3–100 μm under low or high temperatures (473–1273 K), under vacuum, and at various observing angles (from 13 to 85 degree) (Alemanno et al. 2021). They apply their technique to build a spectral database for planetary material analogs and interpret spectroscopic data from orbiters, such as for Mars (Alemanno et al. 2023) and Venus (Helbert et al. 2017). More recently, the University of Pittsburgh (Pittsburgh, USA) developed a micro-furnace integrated to a FTIR spectrometer to measure thermal emission in wide spectral (2.5–20 μm) and temperature (473–1573 K) ranges (Thompson et al. 2021). Their dataset is used for improving lava flow remote sensing to lower the associated risk (Thompson and Ramsey 2021).

Moreover, microscopy coupled with FTIR spectroscopy is frequently used to characterize the mid-IR optical properties of materials at the microscale and room temperature, including the reflectivity and transmissivity of minerals, melt inclusions, and volatiles. Della Ventura et al. (2010) demonstrated how FTIR imaging at micrometer scales can resolve chemical zoning and species within crystals and inclusions. The resulting spectra reveal vibrational features, including Reststrahlen bands and the Christiansen feature (CF), that characterize the interaction of minerals with infrared radiation. Bureau et al. (1998) used micro-FTIR reflectance spectroscopy to measure the water content of melt inclusions approximately 20 μm in diameter hosted in olivine, pyroxene, and plagioclase. Chen et al. (2015) provided a comprehensive review of microscale spectral analysis. Similarly, Storz et al. (2024) measured the mid-IR reflectivity of extraterrestrial carbonaceous materials and showed that subtle mineralogical differences among hydrated carbonaceous samples can be distinguished spectroscopically. Weber et al. (2023) investigated the spectroscopic differences between surfaces of silicate mixtures following laser irradiation.

These studies demonstrate that microscale spectral measurements can resolve variations in mineralogy, chemical composition, and surface properties that may not be captured by bulk measurements. Although spectra of individual phases can be linearly combined to approximate the

article in press

spectral response of a heterogeneous material, this approach may not fully represent its radiative behavior in its natural microstructure. Measuring individual phases within the complex material provides information on their spatial distribution and local heterogeneity. Furthermore, all the studies discussed above were conducted at the microscale without *in situ* high-temperature characterization. Combining microscale resolution with high-temperature measurements would enable the investigation of how mineralogical heterogeneity and evolving surface properties influence spectral emissivity under conditions more representative of active magmatic systems. This approach could improve the interpretation of thermal infrared remote-sensing observations of volcanic surfaces, where temperature, mineralogy, and surface texture all influence the measured signal.

While previous work has been impactful, the capability to measure the radiative properties of rock/molten materials using a combination of high temperature (>1200 K) and microscopic observations is still very limited. With this motivation, we designed a new analytical set-up to measure thermal emission of materials at temperatures above their melting point. This is challenging mostly due to the solid-liquid phase transition and its inherent physical transformation occurring during experiments. Having access to the microscale of such transitions would allow us to observe the different physical behavior of complex materials with changing temperature in greater detail.

Here, we describe the new analytical setup capable of measuring spectral emissivity at high temperature (up to 1773 K) under a microscope. We provide protocols for instrumental calibration and estimates of the sample surface temperature. We validated its performance by comparing our experimental results with existing literature. Finally, we discuss the limitations of the techniques and suggest future steps.

Principles and approaches for spectral emissivity measurementsIn the laboratory, spectral emissivity at room temperature is commonly derived from hemispherical radiative properties using Kirchhoff's laws. In terms of hemispherical reflectance (ρ) and transmittance (τ), the emissivity (ε) can be written as:

article in press

$$\varepsilon(\lambda,T) = 1 - \rho(\lambda,T) - \tau(\lambda,T) \quad \text{Eq. 1}$$

Note that for opaque materials with $\tau = 0$, ε relies primarily on hemispherical ρ measurement. For partially transparent materials such as some SiO_2 allotropes, transmittance must be explicitly accounted for. The hemispherical quantities are integrated over all directions and therefore do not depend on the angle θ. The main limitation of this indirect method at high temperature is the difficulty to occult/differentiate the sample and background thermal emission. Hence in this work, spectral emissivity at high temperature is measured directly through the ratio between the near normal spectral radiance of the sample and that of a blackbody reference in same thermal, and spectral conditions (e.g., Stefan 1879; Boltzmann 1884; De Sousa Meneses et al. 2015; Biren et al. 2022), such as:

$$\varepsilon_x(\lambda,T) = \frac{L_x(\lambda,T)}{L^0_{BB}(\lambda,T)} \quad \text{Eq. 2}$$

While hemispherical emissivity generally differs from directional emissivity for dielectric materials, comparison with hemispherical data is performed here as a first order approximation to validate near normal emissivity measurement at high temperatures, since angular emissivity variations are minimal near normal emission (Howell et al. 2020). Measuring the normal spectral radiance of a surface of an emitter can be challenging due to the presence of additional contributions from the surrounding/background that overlap with the sample emission. The background contribution can come from the environment, the different elements surrounding the sample, as well as the instrument itself. Moreover, the background emission can be sample-dependent (interaction with the sample through scattering or reflection), temperature-dependent (instrument components are heated by the hot sample), and wavelength-dependent (change of sample optical properties). Therefore, the measured normal spectral radiance of the surface of an emitter, L_x, in thermal equilibrium at temperature T and wavelength λ, can be written as:

$$L_x(\lambda,T) = m(\lambda)\,[\varepsilon_x(\lambda,T)\,L^0_{BB}(\lambda,T) + B_x(\lambda,T)] \quad \text{Eq. 3}$$

where $m(\lambda)$ is the system response function, $\varepsilon_x(\lambda,T)$ is the emissivity of the sample x at wavelength

article in press

λ (µm) and temperature T (K), and $B_x(\lambda, T)$ the background in the same conditions. $L^0_{BB}(\lambda, T)$ is the blackbody radiation distribution given by Planck's law, and can be written:

$$L^0_{BB}(\lambda, T) = \frac{2hc^2}{\lambda^5} \frac{1}{e^{\frac{h}{\lambda k_b T}} - 1} \quad \text{Eq. 4}$$

where h, c, k_b, T are respectively the Planck constant (6.62607×10^{-34} J s), speed of light in vacuum (2.99792458×10^8 m s^{-1}), the Boltzmann constant (1.38065×10^{-23} J K^{-1}), and temperature (K).

Based on these theoretical elements and considering the wide temperature range explored in our laboratory settings and the natural temperature dependence of silicate-rich materials (e.g., magmas), two studies are central to the spectral calibration used here. Xiao et al. (2020) give general guidelines for thermal-emission measurements with an FTIR spectrometer. They choose the method according to how large the background is and whether the emissivity changes with temperature. Their "full calibration" first derives the system response from a reference of known emissivity measured at two temperatures. It then separates the background into a sample-independent part and a part that depends on the sample, through its reflectance. This separation uses two references with known emissivity and reflectance.

Ren et al. (2016) describe a high-temperature FTIR emissivity apparatus covering 1073–1873 K and 2–25 µm. They use two variable-temperature blackbody cavities (emissivity above 0.995) as references to obtain the system response and the instrument background, which they express in instrument signal units. They test how the temperature interval between the two blackbody measurements affects the calibration, and they verify detector linearity by comparing the measured blackbody signal with the calculated Planck radiance at several temperatures. When extracting the sample emissivity, they also account for radiation from the surrounding chamber reflected by the sample. Both studies therefore calibrate the system response and the background, but they define and express the background differently and rely on different references. We followed both papers to calibrate our setup: we followed the calibration methods of Ren et al. (2016) for the detector linearity,

article in press

background evaluation, and system response, and the calibration methods of Xiao et al. (2020) for the background evaluation and system response. We then follow De Sousa Meneses et al. (2015) to estimate the temperature of the blackbody reference and sample and to measure the thermal emission of a sample using their "three interferograms" method. A detailed description of the analytical set-up and the calibration is presented in the following section.

article in press

2 Methods

2.1 Sample preparation

To capture the effect of composition on the optical properties of natural dielectric materials without dealing with their complex mineralogy, the materials must be pure or be initially melted to obtain homogeneous crystal-free glass equivalents. To validate the accuracy of the new setup, a SiO_2 pure crystal was purchased online and prepared following Biren et al. (2022): the crystal was drilled to recover cores with 3 mm diameter that were cut into 1.0 ± 0.1 mm thick slices with parallel surfaces. Both faces of each wafer were optically polished to optimize the sample response during IR experiments.

Two blackbody references were selected and prepared: i) a graphite sample with theoretical high emissivity that matched the sample dimensions. The graphite (purity >99 %) was cut into 5.0 ± 0.1 mm diameter × 3.0 ± 0.1 mm thickness and polished, then a 0.8 mm pinhole was drilled in the center of the graphite sample. ii) The second blackbody reference was $LaCrO_3$ (purity 99.5 %) prepared by using powder from BeanTownChem® that was further powdered to <20 μm and then molded through pressure using a compression die to obtain the dimensions of 3.0 ± 0.1 mm diameter × 1.0 ± 0.1 mm thickness. The $LaCrO_3$ pellet was then put in a furnace at 1123 K and sintered at 1623 K for 48 h. The final sample disk was then polished. Independent measurements of the spectral emissivity of these materials are available in the literature over wavelength and temperature ranges relevant to the present study (Wang et al. 2014; De Sousa Meneses et al. 2015; Ren et al. 2016; Zhang et al. 2022).

2.2 Analytical set-up and Measurements

A schematic representation of the experimental set-up is given in Figure 1. The analytical set-up consists of three key elements: a Linkam stage TS1500, a Bruker Hyperion 2000 microscope, and a Bruker FTIR Vertex 80 spectrometer. The Linkam stage holds and heats the sample to the desired temperature while being placed under the microscope connected to the spectrometer measuring the emission signal. The experimental device is placed in an air-conditioned room with controlled

article in press

humidity (~30 %) and temperature (~295 K), to stabilize the environmental conditions of the detector.

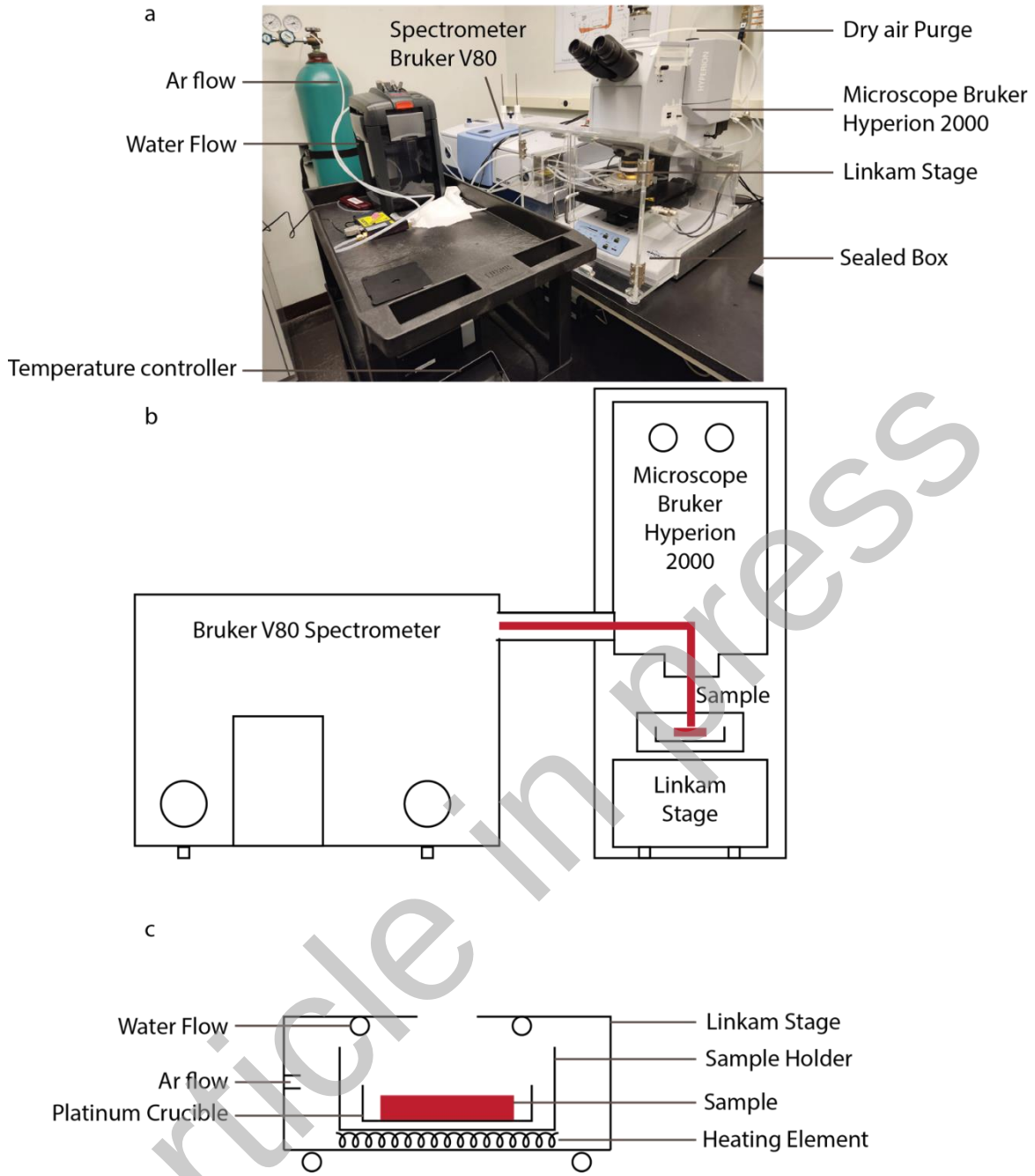


Figure 1: a) Picture representation of the emissivity analytical set-up including the Bruker V80 spectrometer, the Bruker Hyperion 2000 microscope and the Linkam stage holding the sample. b) Schematic representation of the three key elements of the experimental set-up. c) Detailed cross-section schematic of the Linkam stage where the sample is placed and heated.

The Linkam stage, schematized in Figure 1c, holds the sample in an alumina heating crucible. Due to the melting potential of the sample and to avoid any damage to the stage, it is placed in a platinum (Pt) crucible, therefore constraining the sample dimensions to maximum 2 mm thickness × 5 mm diameter. When the sample is heated, the stage temperature is assessed with a thermocouple

article in press

233 embedded in the alumina crucible that is connected to a temperature controller. The temperature of
234 the Linkam stage was calibrated against the melting point of known references (1074 K for NaCl and
235 1337 K for gold) to assure that the temperature set by the temperature controller is the actual
236 temperature in the sample holder. This test was carried out successfully with precision better than 10
237 K. A maximum temperature of 1773 K can be reached with a rapid heating ramp (as high as
238 200 °C min^{-1}) and temperature equilibration within a minute (i.e., the Linkam display confirms the
239 sample isothermal condition). The real sample surface temperature, however, is precisely measured
240 using the Christiansen Feature (described below). This configuration, even if in contact with the
241 sample, is supposed to allow for homogeneous radial and axial heating of the sample. Surrounding
242 the sample holder are the aluminum case and lid that are both kept at low temperature with a water
243 flow cooling system that starts flowing for every experiment hotter than 300 K. The lid allows the
244 sample environment to be open (no window) or close (with an IR-transparent window). Adding an
245 IR-transparent window (KBr, CaF_2 SiO_2; the type of window depends on the maximum temperature
246 to be reached and spectral range to be observed) and eventually an alumina shield (pinhole of 1 mm)
247 on top of the sample holder gives more control on the environment but with the constraint of a more
248 complex optical system. During our experiments, the sample holder remained open and
249 environmental conditions were kept stable by purging it at 60 mL min^{-1} with Ultra-High Purity Argon
250 gas. The emitted signal from the heated sample is captured by the microscope located above the
251 Linkam stage and transmitted to the spectrometer (Figure 1b).

252 The microscope is a Brucker Hyperion 2000 with a single ×15 objective purged with dry air (with
253 Numerical Aperture of 0.4 and optical resolution of 4–20 μm). To minimize optical aberration, the
254 light beam path between the microscope and the detector is kept simple: the light emitted by the
255 sample is gathered at normal incidence by the microscope objective and then directed towards the
256 spectrometer by a set of four mirrors. Despite the open configuration of the Linkam stage, we assume
257 that the ×15 objective is not impacted by the radiating heat from the sample and is accounted in the

article in press

system's background calibration. The choice of an adequate aperture (which can be changed from 0.5 up to 2.5 mm by 0.5 mm increment) depends on sample size and temperature homogeneity to perform accurate measurements. In regular configuration, a 1- or 2 mm aperture is used. To improve the environmental stability of the analytical set-up, the optical system is placed into a sealed polymer enclosure purged with dry air to maintain low levels of atmospheric water vapor and CO_2 during experiments (Fig. 1a). The Bruker Vertex 80 spectrometer that is connected to the microscope is also dry air purged.

The Bruker Vertex 80 spectrometer is equipped with two detectors, a Mercury Cadmium Telluride (MCT) and a Deuterated Lanthanum α Alanine doped TriGlycine Sulphate (DLaTGS), covering the far–near infrared spectral range (1.2–28.6 μm). In practice, the detector of choice and its corresponding beamsplitter (KBr) is set using the software OPUS. The source is set as "Hyperion Emission Measurement" in OPUS software to adjust the light beam path from the microscope to the spectrometer for capturing the sample emission. There is no specific optical path or measuring configuration for the blackbody reference as it is commonly done with industrial blackbody furnaces. Instead, the blackbody reference is considered a regular sample and is measured in the same experimental conditions as the sample of interest. Using an identical optical path improves the measurement precision and data quality.

Evolution of spectral emissivity with temperature was measured *in situ* using the analytical set-up described above. The blackbody reference and the sample of interest were measured on separate days due to the long duration of the individual experiments over the whole temperature range. In this experimental configuration (see also Eq. 2) the thermal emission of the instrument and background contribution, the blackbody reference and the sample are collected individually every 50–100 K from 600 K to 1773 K (for a total of ~24 steps). Measurement at each temperature step takes ~20 min for a total of ~8 h for an individual sample experiment. A purging time of 45–120 min before each experiment is respected, and in addition, a standing period of at least three minutes is applied at each

article in press

283 temperature step assuring homogeneous temperature of the sample before measurement. The
284 blackbody reference is first measured for the whole temperature range, then the stage is rapidly cooled
285 (a few minutes) and the reference is removed. The following day, the sample is placed in the sample
286 holder, purged and measured following the same steps in similar optical, thermal, and spectral
287 conditions. To eliminate the background contribution, the method of three interferograms developed
288 by De Sousa Meneses et al. (2015) derived from Planck's law is applied:

$$\varepsilon_x(\lambda,T) = \frac{FT(I_x - I_a)}{FT(I_{BB} - I_a)} \frac{L^0_{BB}(\lambda,T) - L^0_a(\lambda,T)}{L^0_x(\lambda,T) - L^0_a(\lambda,T)} \varepsilon_{BB}(\lambda,T) \quad \text{Eq. 5}$$

article in press

where I_a, I_{bb}, I_x are the interferograms (acquired with 64 scans using MCT and 320 scans using DLaTGS, depending on the choice of detector) and L_a^0, L_{bb}^0, L_x^0 are the Planck functions of the ambient background contribution, the blackbody reference and the sample, respectively. ε_{BB} is the emissivity of the blackbody reference. The thermal emissions of the sample and the blackbody reference are collected at each temperature step from 673 K to 1773 K and the sample was quenched afterwards by shutting down the Linkam heating stage. The thermal emission of the ambient background was collected at room temperature (295 K) and considered constant at every temperature step. Note that the temperature set by the heating stage during the experiment only gives an approximate value. Therefore, the precise temperature of the sample surface is not defined by the Linkam stage but is radiometrically calculated (~98% of accuracy, see Brun 2003; Eckes et al. 2013) using the Christiansen Feature (Rozenbaum et al. 2009; De Sousa Meneses et al. 2015; Li et al. 2021; Biren et al. 2022). At this specific wavelength, the emissivity of the dielectric approaches unity and the spectral radiance is primarily controlled by temperature. Therefore, the FTIR spectrometer effectively operates as a monochromatic pyrometer (at the CF wavelength), and the sample temperature can be retrieved using Planck's law. Under these conditions, the standard uncertainty in the determination of the material temperature is estimated to be less than 1% (or 10–20 K). Once emissivity spectra are calculated, remaining contributions from H_2O (5.25–5.32 µm;) and CO_2 (14.7–15.30 µm, 4.19–4.33 µm) are corrected for by applying a linear baseline between the spectral regions immediately adjacent to each absorption band. The baseline is then subtracted from the corresponding spectral region to remove the contribution of these atmospheric volatiles. The final corrected spectrum is smoothed using a 20-point smoothing window. This smoothing is applied primarily to reduce noise at the boundaries of the spectral range, where the detector response and signal-to-noise ratio are lower, while ensuring that no significant spectral features are removed or altered.

article in press

2.3 Calibration

2.3.1 System Calibration

For an accurate measurement, it is critical to record a signal while knowing the relation between the radiation intensity striking the detector and the electrical response of the instrument precisely (Lachance 2000). Therefore, we followed the calibration methods of Ren et al. (2016) for the detector linearity, background evaluation, and system response, and the calibration methods of Xiao et al. (2020) for the background evaluation and system response. Following Ren et al. (2016), the detector response in function of the incident radiant intensity is obtained between the measured blackbody reference signals (Graphite/$LaCrO_3$) and the calculated blackbody radiation (Planck's law) at different temperatures. The results between 373 and 1773 K, presented in Figure 2, indicate a clear linear fit at 10 µm showing that the incident radiance remains within the linear dynamic range of the detector at this wavelength. In contrast, slight deviations from linearity are observed at 3 µm and 20 µm, which are attributed to reduced signal levels and optical throughput at the spectral limits of the interferometer–detector system. At 3 µm, a polynomial fit constrained to remain positive was used to avoid the physically unrealistic negative values that could result from linear extrapolation. Although the measured calibration curves do not exhibit perfect linearity at all wavelengths, the deviations from linear behavior remain small over the investigated radiance range. For spectral emissivity determination, the detector response is therefore approximated as linear, consistent with common practice (Carter et al. 1990). To evaluate detector stability, the spectral emission of a reference was measured at a given temperature (1273 K) every 30 min for a period that is equivalent to the usual experiment time (~8h). This shows that the detectors show extremely good stability with emissivity variation through time by <0.02 units in the studied spectral range.

article in press

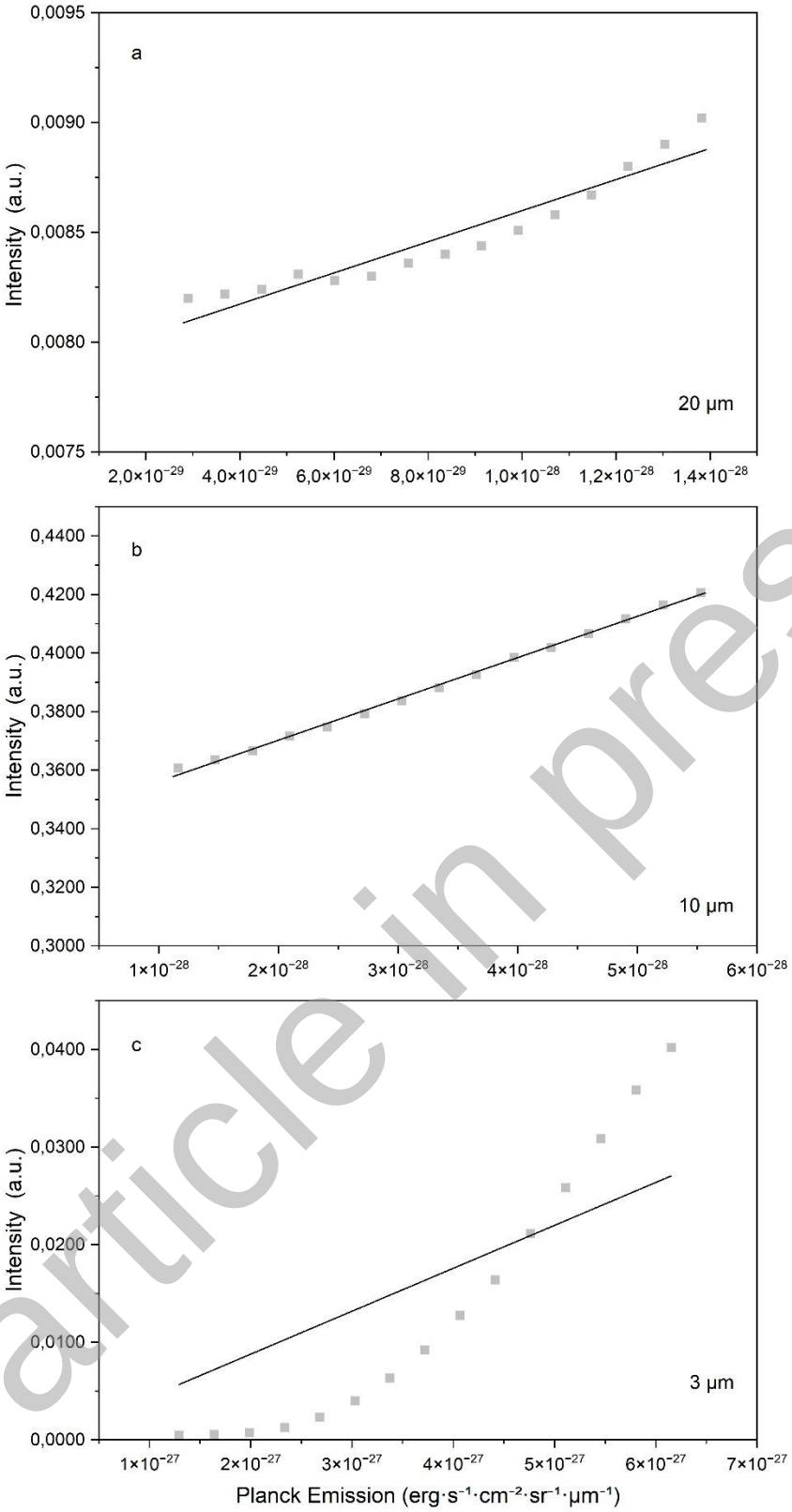


Figure 2: Linear fit of the detector signal intensity over the detected Planck Emission through the temperature range 373–1773 K at a-20 µm, b- 10 µm , and c- 3 µm.

article in press

The calibration method of Xiao et al. (2020) allows to characterize almost any emission measurement. From the simplest calibration methods of (Xiao et al. 2020), the background is non negligible and SiO_2 is temperature dependent (described in Suppl Mat; link to Zenodo depository: https://zenodo.org/records/17179535?preview=1&token=eyJhbGciOiJIUzUxMiIsImlhdCI6MTc2ODMwNDIyMywiZXhwIjoxNzc3NTA3MTk5fQ.eyJpZCI6IjczYTg1Nzg3LTc1OTEtNDA3My1hOTIxLWNkNGQyZWM4Nzk5ZCIsImRhdGEiOnt9LCJyYW5kb20iOiI0YTdkZmIyMjQ2MDFiOWRhZDNmMGE1ZjNkYzNhMWZmYiJ9.wsCEBSzYq17bl-mmIUj9muDivsDRF0MiLLYDkIyLlNwQ2dqf4-njJsAryWKZJwYuUToVp9Z8Vr_yYBU3KfN5WA). Therefore, only a comprehensive calibration of the analytical setup will allow us to retrieve the T-dependent emissivity data. The calibration method of Xiao et al. (2020) allows the extraction of the samples' true emission, $L_x^0(\lambda, T)$, by first fully characterizing the system response, $m\ (\lambda)$, and the background, $B_x(\lambda, T)$, as:

$$L_x^0(\lambda, T) = \frac{L_x(\lambda, T)}{m\ (\lambda)} - B_x(\lambda, T) \qquad \text{Eq. 6}$$

The system response function $m\ (\lambda)$ can be obtained by using the thermal-emission signal measured from a known reference α whose optical properties do not change with temperature at two different temperatures T_1 and T_2:

$$m\ (\lambda) = \frac{L_a(\lambda, T_1) - L_a(\lambda, T_2)}{\varepsilon_\alpha(\lambda)\ [L_{BB}^0(\lambda, T_1) - L_{BB}^0(\lambda, T_2)]} \qquad \text{Eq. 7}$$

For an opaque and non-scattering emitter x, the sample dependence of background is expected to be entirely due to light reflected by the sample into the beam path. Therefore, the background $B_x(\lambda, T)$ can be written as:

$$B_x(\lambda, T) = B_1(\lambda) + \rho_x(\lambda, T)\ B_2(\lambda) \qquad \text{Eq. 8}$$

where $B_1(\lambda)$ represent the sample-independent component of the background, and $\rho_\lambda(\lambda, T)\ B_2(\lambda)$ the sample-dependent component with $\rho_\lambda(\lambda, T)$ the reflectance of the emitter x, respectively. To

article in press

characterize $B_1(\lambda)$ and $B_2(\lambda)$, at least non-scattering reference samples (α and β) with known temperature-independent emissivities $\varepsilon_{\alpha,\beta}(\lambda)$ and reflectances $\rho_{\alpha,\beta}(\lambda)$ are required. The total background for the reference samples α and β can be obtained from the measured thermal emission spectra at a given temperature T_1:

$$B_\alpha(\lambda, T_1) = \frac{L_\alpha(\lambda, T_1)}{m\,(\lambda)} - \varepsilon_\alpha(\lambda) L^0_{BB}(\lambda, T_1) \quad \text{Eq. 9}$$

$$B_\beta(\lambda, T_1) = \frac{L_\beta(\lambda, T_1)}{m\,(\lambda)} - \varepsilon_\beta(\lambda) L^0_{BB}(\lambda, T_1) \quad \text{Eq. 10}$$

Then, $B_1(\lambda)$ and $B_2(\lambda)$ can be calculated using Eq. 8, such as:

$$B_2(\lambda) = \frac{B_\alpha(\lambda) - B_\beta(\lambda)}{\rho_\alpha(\lambda) - \rho_\beta(\lambda)} \quad \text{Eq. 11}$$

$$B_1(\lambda) = B_\alpha(\lambda) - \rho_\alpha(\lambda)\, B_2(\lambda) \quad \text{Eq. 12}$$

We used $LaCrO_3$ and Graphite as reference samples to characterize the background $B_x(\lambda, T_1)$, because both references are opaques and have negligible scattering in the spectral range 5–14 μm. Figure 3 shows the system function response $m\,(\lambda)$ of our setup using Eq. 7 using both references at two temperatures (773–873 K and 1173–1273 K). The system response is proportional to detected photon counts; uncertainties and therefore follows Poisson statistics. The response at two temperatures is identical in the range 5–15 µm (the signal variation is less than 1×10^{-10}), as expected. However, both references start to show different system function responses in the high wavelength part of the spectrum (>15 µm) that is due to the temperature dependence of their lattice vibrations inducing a non-negligible evolution of its emissivity, as demonstrated in Suppl Mat. (Fig. 3, Zenodo link https://zenodo.org/records/17179535?preview=1&token=eyJhbGciOiJIUzUxMiIsImlhdCI6MTc2ODMwNDIyMywiZXhwIjoxNzc3NTA3MTk5fQ.eyJpZCI6IjczYTg1Nzg3LTc1OTEtNDA3My1hOTIxLWNkNGQyZWM4Nzk5ZCIsImRhdGEiOnt9LCJyYW5kb20iOiI0YTdkZmIyMjQ2MDFiOWRhZDNmMGE1ZjNkYzNhMWZmYiJ9.wsCEBSzYq17bl-mmIUj9muDivsDRF0MiLLYDkIyLlNwQ2dqf4-njJsAryWKZJwYuUToVp9Z8Vr_yYBU3KfN5WA), and De Sousa Meneses et al. (2015). Thus, the

article in press

system is only temperature independent below <15 μm, which mark the upper spectral limit of our system. It is known that Mid-IR detectors work best >2.5 μm, marking the lower spectral limit of our system.

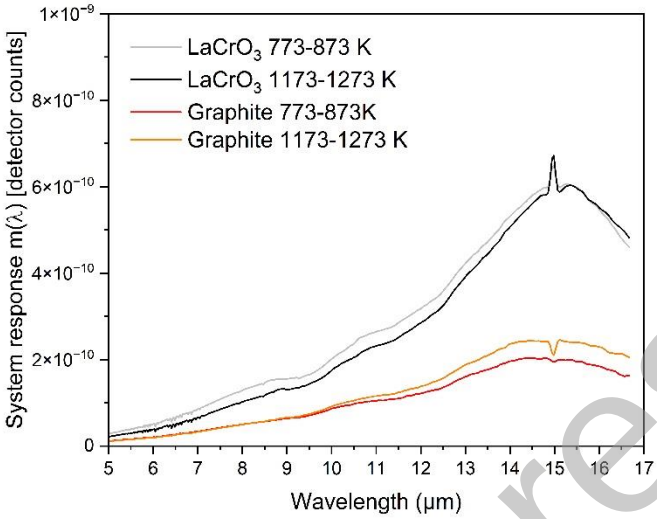


Figure 3: System response function for two blackbody references ($LaCrO_3$ and Graphite) at two temperature intervals following Eq. 7. derived from Xiao et al. (2020) calibration.

Figure 4 shows the measured total background for two blackbody references, $LaCrO_3$ and graphite (see Eq. 8). In the optical path of our instrument, components located between the sample and the interferometer are referred to as being "before" the interferometer, whereas components located between the interferometer and the detector are referred to as being "after" the interferometer. Both references exhibit positive background values, indicating a net background contribution from components before the interferometer that emit or reflect radiation towards it. Furthermore, the total background differs between the two references, indicating that $B_2(\lambda) \neq 0$.

article in press

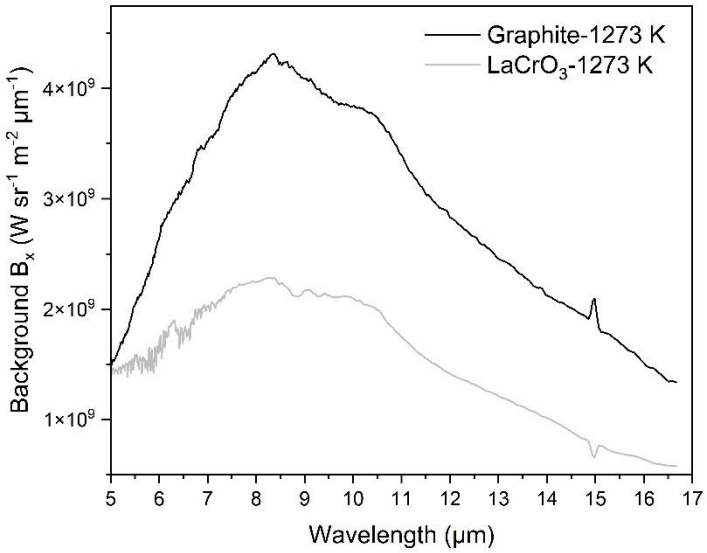


Figure 4: Background measurement for two blackbody references (B_x, where x = Graphite or $LaCrO_3$) at 1273 K using (Xiao et al. 2020) calibration.

Figure 5 shows the spectra of $B_1(\lambda)$ and $B_2(\lambda)$ calculated using Eq. 12 and Eq. 11, respectively. Both $B_1(\lambda)$ and $B_2(\lambda)$ are positive and close to zero, indicating that they mainly originate from optical components before the interferometer and contribute only a small fraction of the total signal. This behavior is expected because the background emitted by these components follows the same optical path as the sample emission, with both signals transmitted through the interferometer before reaching the detector (Xiao et al. 2020). In contrast, negative values indicate that $B_1(\lambda)$ originates from optical components located after the interferometer. This radiation is detected after being reflected by the interferometer rather than transmitted through it and therefore does not interact with the sample. As a result, this component is independent of the sample properties (Xiao et al. 2020).

article in press

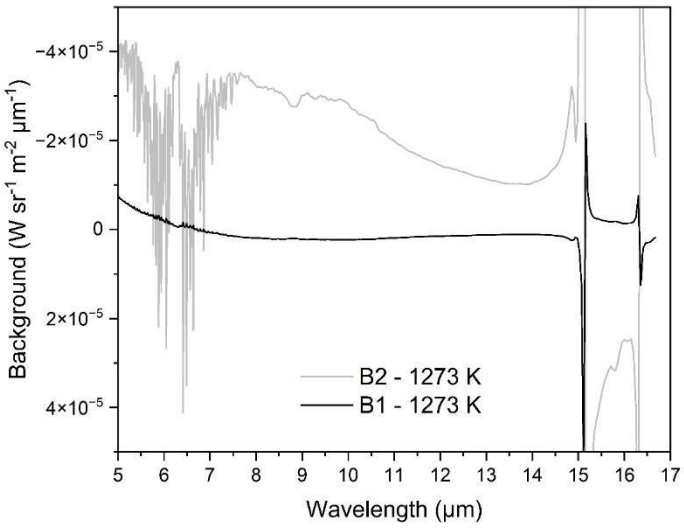


Figure 5: Measurements from Eq. 11 and 12 as to obtain parameters $B_1(\lambda)$ and $B_2(\lambda)$ at 1273 K using $LaCrO_3$ and Graphite as two blackbody references (see text).

Similarly to the calibration of Xiao et al. (2020), the system response function was determined for different temperatures (from 773 to 1573 K) and temperature intervals ($\Delta T = 100\ to\ 500$ K) for the two references ($LaCrO_3$ and Graphite) using the calibration of Ren et al. (2016). Figure 6 shows the calibration results for $\Delta T = 100\ K$ at 873 and 1273 K. The results from this calibration method (Ren et al. 2016) confirm a good agreement over the entire spectral range between references, especially <15 µm, further implying that the system response is temperature independent in that spectral range. The difference in the background spectra and intensities (Figure 4 and 6b) is mainly due to the different definitions used in the two calibrations. Xiao et al. (2020) express the background in radiance units (W m^{-2} sr^{-1} m^{-1}), after dividing the signal by the system response and subtracting the emissivity-weighted blackbody term of the reference, ($\varepsilon_\alpha(\lambda)$). Ren et al. (2016) report the background in arbitrary signal units, which implicitly assumes ε = 1 for their blackbody references.

article in press

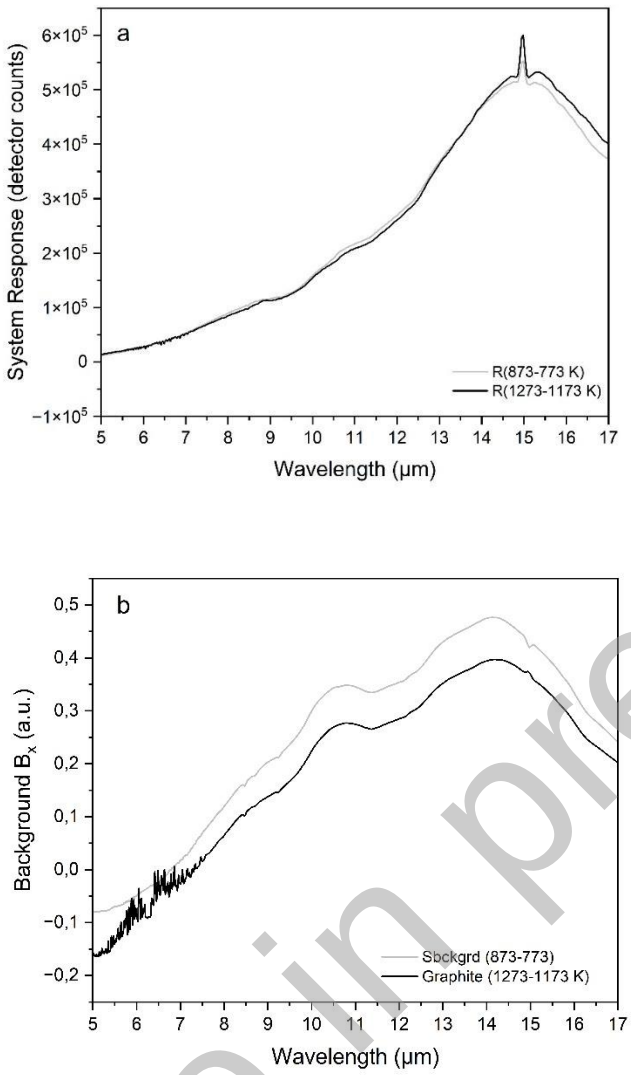


Figure 6: a) System Response for a given delta temperature (100 K) at 873 and 1273 K, and b) total background contribution for two blackbody references ($LaCrO_3$ and Graphite) at 1273 K using Ren et al., (2016) calibration. Peaks at ~15 μm are CO_2 absorption.

2.3.2 Blackbody Reference Temperature Estimation

Accurate emissivity measurements depend critically on the quality of the blackbody reference and the precise determination of its temperature. The precise measurement of the blackbody temperature is challenging for this set-up, and different methods to obtain the best temperature estimate were used. We applied three methods: i) using a thermocouple, ii) using a thermal camera and iii) using mathematical regression from the blackbody temperature calibration (De Sousa Meneses et al. 2015).

article in press

The results of temperature estimation using the different methods are shown in Suppl. Mat (link to Zenodo depository: https://zenodo.org/records/17179535?preview=1&token=eyJhbGciOiJIUzUxMiIsImlhdCI6MTc2ODMwNDIyMywiZXhwIjoxNzc3NTA3MTk5fQ.eyJpZCI6IjczYTg1Nzg3LTc1OTEtNDA3My1hOTIxLWNkNGQyZWM4Nzk5ZCIsImRhdGEiOnt9LCJyYW5kb20iOiI0YTdkZmIyMjQ2MDFiOWRhZDNmMGE1ZjNkYzNhMWZmYiJ9.wsCEBSzYq17bl-mmIUj9muDivsDRF0MiLLYDkIyLlNwQ2dqf4-njJsAryWKZJwYuUToVp9Z8Vr_yYBU3KfN5WA). We found that neither the thermocouple, nor the thermal camera produced reliable results; the K-type thermocouple does not reach the temperatures required for this study and the thermal camera relies on the knowledge *a priori* of the reference emissivity. Thus, the best method to evaluate the blackbody temperature is based on mathematical regression to determine the thermodynamic temperature (i.e., physical temperature governing thermal radiation), T_{BB}, of the flux emitted by the blackbody reference (De Sousa Meneses et al. 2015). This procedure was applied for the blackbody reference $LaCrO_3$ using the Linkam stage as the supplementary thermometer required for this method. The Linkam stage has a linear response, and the blackbody reference has no temperature-dependency in the thermal and spectral range explored – as explained in the system calibration section. The procedure requires measuring the thermal emission of the blackbody sample, L_{BB}, at three temperatures: the temperature T_{BB} at which the reference needs to be calibrated, a colder temperature ($T_{BB} - \Delta T_{BB}$) and a hotter temperature ($T_{BB} + \Delta T_{BB}$). The following ratios are then calculated:

$$R^{-}_{\Delta T_{BB}}(\lambda) = \frac{L_{BB}(T_{BB} - \Delta T_{BB})}{L_{BB}(T_{BB})} \quad \text{Eq. 13}$$

$$R^{+}_{\Delta T_{BB}}(\lambda) = \frac{L_{BB}(T_{BB} + \Delta T_{BB})}{L_{BB}(T_{BB})} \quad \text{Eq. 14}$$

These ratios allow to eliminate both the system response function and calculate the true emissivity of the blackbody reference. The next step is to fit the ratios with the following model:

article in press

$$R_p^{T\pm\Delta T}(\lambda) = \frac{exp\ exp\left(\frac{hc}{\lambda kT}\right) - 1}{exp\ exp\left[\frac{hc}{\lambda k(T \pm \Delta T)}\right] - 1} \quad \text{Eq. 15}$$

The fit is realized by minimizing the following objective function:

$$g(T) = \sum_{i=0}^{N} \left[\left(R_p^{T(1+A)}(\lambda_i) - R^{+}_{\Delta T_{BB}}(\lambda_i)\right)^2 + \left(R_p^{T(1-A)}(\lambda_i) - R^{-}_{\Delta T_{BB}}(\lambda_i)\right)^2\right] \quad \text{Eq. 16}$$

with $A = \frac{\Delta T_{Linkam}}{T_{Linkam}} = \frac{\Delta T_{BB}}{T_{BB}}$ is is the relative temperature interval used in the optimization (following De Sousa Meneses et al. 2015). Here, T_{Linkam} is the temperature measured by the Linkam stage, and ΔT_{Linkam} is the temperature interval selected for calibration. The equality between the relative temperature intervals of the Linkam stage and the blackbody reference is an assumption of the method, rather than an independently measured relationship. The optimization problem has a single adjustable parameter, the thermodynamic temperature T_{BB} of the blackbody reference, which is determined by minimizing the objective function. The method was applied to the $LaCrO_3$ blackbody reference for each Linkam temperature setting (T_{Linkam}), from 773 to 1573 K by 100 K increments, using a temperature interval (ΔT_{Linkam}) of 200 K and a spectral range of 2.5–4 µm. Figure 7 shows the results of the optimization (best fits) for a Linkam temperature setting of 1273 K for which, the thermodynamic temperature of the blackbody reference is equal to 1297 K.

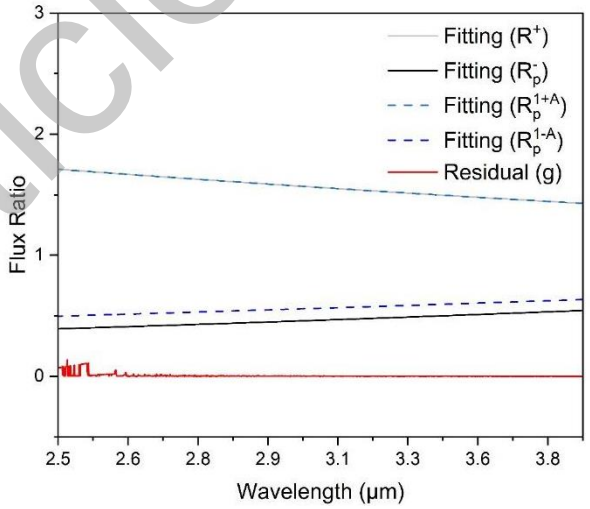


Figure 7: Best fits of the experimental ratios of fluxes emitted by the blackbody reference. T_{Linkam} is equal to 1273 K and $\Delta T_{Linkam} = 200\ K$. The dash curves represent Planck ratios (Eq. 15, see text) obtained for a temperature T_{BB} equal to 1297 K.

article in press

3 Results and Discussion

3.1 Spectral Emissivity of SiO_2 (Crystalline)

To validate emissivity results obtained with our new setup, a set of normal spectral emissivity spectra for a quartz (a common silicate in volcanic rocks) was acquired using both direct and indirect methods. Figure 8 compares the spectral emissivity of SiO_2 crystal determined indirectly using spectral reflectivity and transmissivity and directly at low temperature (462 K). Once the data obtained at room temperature are inverted using Eq. 1, they are in good agreement with direct emissivity at 462 K. Therefore, it shows a first order approximation between indirect and direct SiO_2 data to validate near normal emissivity measurement at higher temperature since angular variations of emissivity are minimal near normal emission. A comparison with emittance values acquired by direct and indirect methods led us to estimate the standard uncertainty of ε measurements to be of 1–2% at the vicinity of the CF and 5% above 2000 cm^{-1} (del Campo et al., 2011). These uncertainties are similar to what is found in literature for IR spectroscopy (Ruff et al. 1997). Note that, when the direct method is applied at relatively low temperature, ε can only be measured in a limited spectral range because of the weak thermal radiation. High temperature emissivity data were acquired with DLaTGS detector and Graphite as blackbody reference.

Emissivity spectra of SiO_2 were studied previously and shows a well-organized mineral structure with numerous, well developed, absorption bands (e.g., Petrov and Reznik 1972; Wenrich and Christensen 1996; Rozenbaum et al. 1999; De Sousa Meneses et al. 2014). They are notably characterized by: 1- well visible wide Reststrahlen double absorption bands (at ~9.09 μm and ~8.47 μm) where emissivity is low (0.23; minimum), 2- the presence of the Christiansen Feature (CF at ~7.38 μm), and a Transmission Front (TF at ~4.92 μm) showing its semi-transparent optical behavior where emissivity drops from >0.95 down to ~0.24. These features are typical of dielectric materials and match previous studies (Petrov and Reznik 1972; Wenrich and Christensen 1996; Rozenbaum et al. 1999; De Sousa Meneses et al. 2014), as demonstrated in Figure 10a. Other minor absorption bands >5 μm are located at ~14.49 μm, and ~12.58 μm where emissivity is relatively high

article in press

(0.84 and 0.68 respectively for each band). Note that the studied mineral was unoriented, preventing the study of orientation effect on the crystal radiative properties with temperature, although literature data clearly show the dependence of emissivity spectra on crystal orientation, (e.g., Eckes et al. 2013; Ye et al. 2019; Li et al. 2021).

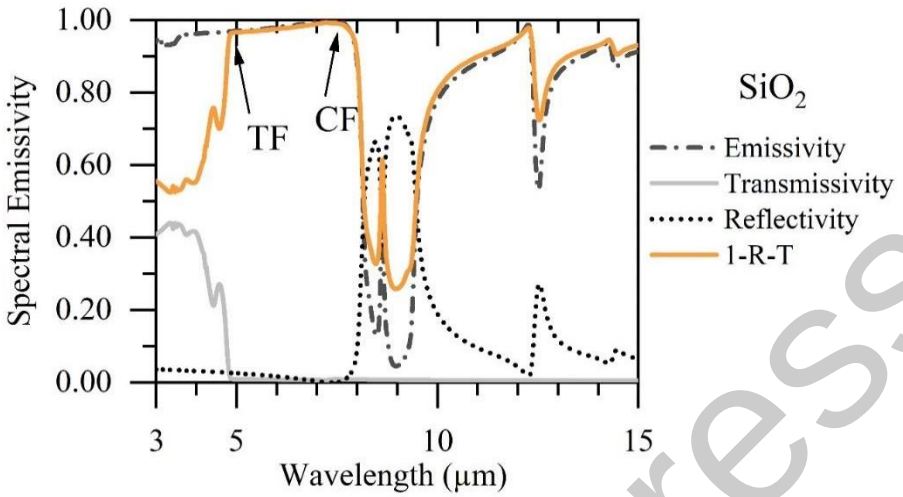


Figure 8: Spectral reflectivity, emissivity transmissivity of a SiO_2 crystal. The indirect emittance spectrum results from the combination of individual reflectance and transmittance spectra (1-R-T) obtained at room temperature and is compared to direct acquisition of its emissivity at 462 K.

Figure 9 shows the spectral emissivity evolution from 600 to 1700 K for the SiO_2 crystal. Even at low temperatures, the signal-to-noise ratio is excellent as is the stability over time. The CF shifts to higher wavelength with increasing temperature (to ~7.63 µm at ~1650 K). The double Reststrahlen bands are reduced to one single broad band with an emissivity minimum that shifts to higher wavelength (to ~9.22 µm) and increases in intensity to ~0.54. The absorption band at ~14.49 µm disappears and the absorption band at ~12.58 µm reduces. The simplification of the structure is related to the transition of alpha quartz to beta quartz which occurs between 772 and 870 K in our data (see also 847 K in De Sousa Meneses et al. 2014). De Sousa Meneses et al. (2014) describes the transition from beta-quartz to cristobalite at 1743 K and to the liquid phase above 1999 K but we could not observe these two transitions because our setup does not reach the required temperature (our maximum temperature is 1654 K).

article in press

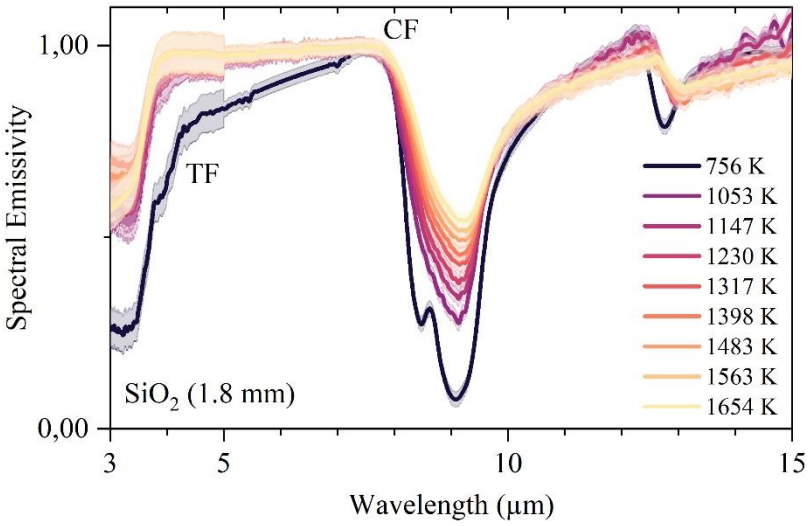


Figure 9: Spectral emissivity evolution with temperature for a SiO_2 crystal.

Our high-temperature results agree well with those of De Sousa Meneses et al. (2014), as shown in Figure 10. The comparison is made using a SiO_2 emissivity spectrum at 1170 K, obtained by linearly interpolating our measurements between 1147 and 1230 K, and the spectrum measured at 1170 K by De Sousa Meneses et al. (2014).. The analytical setups are similar in that they measure the normal spectral emissivity of the sample but differ in their field of view; while De Sousa Meneses et al. (2014) setup looks at the macroscale, ours was specifically developed for microscopy. The temperature and spectral ranges covered by our setup are within the ones from De Sousa Meneses et al. (2014). However, having similar results at the microscale and macroscale validate our measurements. Our measurements can also be compared with other recent investigations of the spectral emissivity of high-temperature geological materials. Thompson and Ramsey (2021) measured the spectral emissivity of minerals and a Hawaiian basalt from 473 to 1573 K over the 2.5–20 µm range using a high-temperature FTIR emission system. Their measurements similarly demonstrate significant temperature-dependent variations in emissivity and spectral features associated with the silicate structure. More recently, Biren et al. (2022) and Fortin et al. (2024) investigated the high-temperature spectral emissivity of basalts from room temperature to 1800 K and 1623 K respectively over the 2.5–25 µm and 2.0–20 µm range respectively. Their results likewise

article in press

demonstrate that emissivity varies with both temperature and material structure. The spectra obtained in the present study are consistent with these observations, while extending the available measurements to microscale measurements. Differences between datasets may arise from variations in sample composition, crystallinity, surface state, measurement geometry, and experimental methodology.

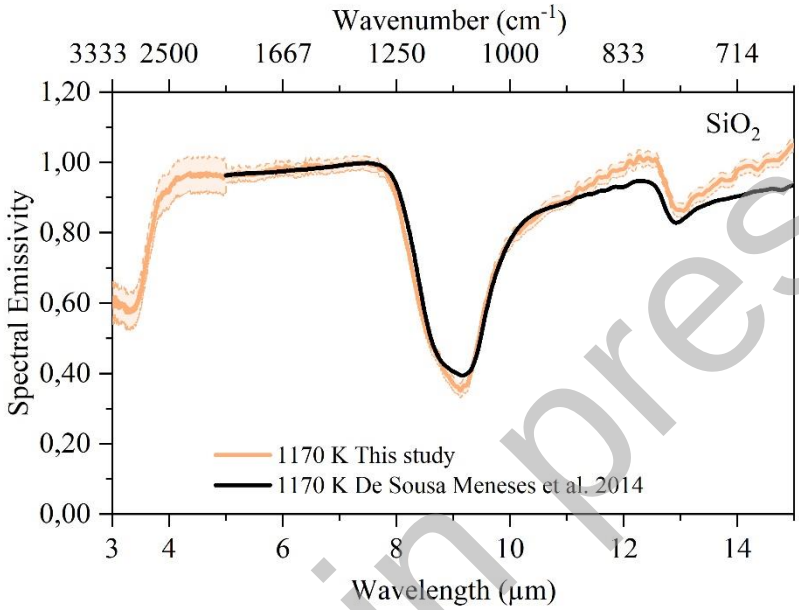


Figure 10: Comparison between HT emissivity data obtained with the new setup at Cornell University and De Sousa Meneses et al. (2014). Data at 1170 K for this study were linearly interpolated from data between 1147 and 1230 K.

article in press

4 Conclusions and Recommendations

We described a new analytical setup that is capable of characterizing the infrared radiative properties of any solid or molten, homogeneous or heterogeneous, opaque or semi-transparent dielectric material. Our microscopic approach can measure the sample radiative properties (spectral emissivity and reflectivity) *in situ*, directly and indirectly, over large temperature (673 to 1773 K) and spectral (from 3 to 15 μm) ranges.

The FTIR spectrometer allows measuring the temperature of the studied surface accurately using the Christiansen point for most of the dielectric materials such as silicates. At lower temperatures the setup is limited by the small size of the emitting material and thus the amount of signal received at the detector, and at higher temperatures by the Linkam stage heating capabilities. The microscope equipped with a ×15 objective has a small optical aperture allowing for potentially capturing the signal of microcrystals (~100 μm). This allows for observing mineral evolution at microscale with temperature and their phase transition, demonstrating a new way to characterize physical processes in magmatic systems.

The temperature-dependent data acquisition helps understand the dynamic behavior near phase transitions and the impact on radiative properties, with potential applications in volcanology and space exploration. Two implementations are recommended for future improvements: exploring different environmental conditions and extending the thermal and spectral ranges. These enhancements will provide complementary information about the sample's structure and composition.

article in press

5 Acknowledgements

The authors would like to thank early reviewers for their insightful comments and guidance during the early stages of this work: We are also grateful to Tom Tague from Bruker and Yuzhe Xiao for their constructive feedback about issues we encountered in the development of this setup.

6 Authors' contributions

JB: writing - original draft, data curation, investigation, formal analysis, methodology.

EG: supervision, funding acquisition, conceptualization, investigation, methodology, writing.

LK: supervision, funding acquisition, conceptualization, investigation, writing.

7 Funding

This study was supported by the Hessing-Simons Foundation and NASA XRP.

8 Data Availability

The original contributions presented in this study are included in the Supplementary Materials on Zenodo depository:

https://zenodo.org/records/17179535?preview=1&token=eyJhbGciOiJIUzUxMiIsImlhdCI6MTc2ODMwNDIyMywiZXhwIjoxNzc3NTA3MTk5fQ.eyJpZCI6IjczYTg1Nzg3LTc1OTEtNDA3My1hOTIxLWNkNGQyZWM4Nzk5ZCIsImRhdGEiOnt9LCJyYW5kb20iOiI0YTdkZmIyMjQ2MDFiOWRhZDNmMGE1ZjNkYzNhMWZmYiJ9.wsCEBSzYq17bl-mmIUj9muDivsDRF0MiLLYDkIyLlNwQ2dqf4-njJsAryWKZJwYuUToVp9Z8Vr_yYBU3KfN5WA.

Further inquiries can be directed at the corresponding author.

9 References

Alemanno G, Carli C, Serventi G, et al (2023) Study of Detection Limits of Carbonate Phases in Mixtures with Basaltic-like Fine Regolith in the MIR (1–5.5 µm) Spectral Range. Minerals 13:764. https://doi.org/10.3390/min13060764

Alemanno G, Maturilli A, D'Amore M, Helbert J (2021) A new laboratory emissivity and reflectance spectral library for the interpretation of Mars thermal infrared spectral data. Icarus 368:114622. https://doi.org/10.1016/j.icarus.2021.114622

article in press

588 Baldridge AM, Hook SJ, Grove CI, Rivera G (2009) The ASTER spectral library version 2.0. Remote Sens
589 Environ 113:711–715. https://doi.org/10.1016/j.rse.2008.11.007

590 Biren J, Slodczyk A, Andújar J, et al (2022) High temperature spectral emissivity of glass and crystal-
591 bearing basalts. J Volcanol Geotherm Res 430:107623.
592 https://doi.org/10.1016/j.jvolgeores.2022.107623

593 Boltzmann L (1884) Ableitung des Stefan'schen Gesetzes, betreffend die Abhängigkeit der Wärmestrahlung
594 von der Temperatur aus der electromagnetischen Lichttheorie. Ann Phys 258:291–294.
595 https://doi.org/10.1002/andp.18842580616

596 Brun J-F (2003) Mesure et analyse de l'émittance spectrale d'oxydes diélectriques à haute température. Une
597 approche des phénomènes préfusionnels. Physique, Université d'Orléans

598 Brun JF, Del Campo L, De Sousa Meneses D, Echegut P (2013) Infrared optical properties of α-alumina with
599 the approach to melting: γ-like tetrahedral structure and small polaron conduction. J Appl Phys 114:.
600 https://doi.org/10.1063/1.4846077

601 Bureau H, Métrich N, Pineau F, Semet MP (1998) Magma–conduit interaction at Piton de la Fournaise
602 volcano (Réunion Island): a melt and fluid inclusion study. J Volcanol Geotherm Res 84:39–60.
603 https://doi.org/10.1016/S0377-0273(98)00029-8

604 Cáceres F, Wadsworth FB, Scheu B, et al (2020) Can nanolites enhance eruption explosivity? Geology
605 48:997–1001. https://doi.org/10.1130/G47317.1

606 Carter RO, Lindsay NE, Beduhn D (1990) A Solution to Baseline Uncertainty Due to MCT Detector
607 Nonlinearity in FT-IR. Appl Spectrosc 44:1147–1151. https://doi.org/10.1366/0003702904086515

608 Chen Y, Zou C, Mastalerz M, et al (2015) Applications of Micro-Fourier Transform Infrared Spectroscopy
609 (FTIR) in the Geological Sciences-A Review. Int J Mol Sci 16:30223–30250.
610 https://doi.org/10.3390/ijms161226227

611 De Sousa Meneses D, Eckes M, del Campo L, Echegut P (2014) Phase transformations of crystalline SiO2
612 versus dynamic disorder between room temperature and liquid state. J Phys Condens Matter
613 26:255402. https://doi.org/10.1088/0953-8984/26/25/255402

614 De Sousa Meneses D, Melin P, del Campo L, et al (2015) Apparatus for measuring the emittance of
615 materials from far infrared to visible wavelengths in extreme conditions of temperature. Infrared
616 Phys Technol 69:96–101. https://doi.org/10.1016/j.infrared.2015.01.011

617 Della Ventura G, Bellatreccia F, Marcelli A, et al (2010) Application of micro-FTIR imaging in the Earth
618 sciences. Anal Bioanal Chem 397:2039–2049. https://doi.org/10.1007/s00216-010-3811-8

619 Di Genova D, Zandona A, Deubener J (2020) Unravelling the effect of nano-heterogeneity on the viscosity
620 of silicate melts: Implications for glass manufacturing and volcanic eruptions. J Non-Cryst Solids
621 545:120248. https://doi.org/10.1016/j.jnoncrysol.2020.120248

622 Eckes M, Gibert B, De Sousa Meneses D, et al (2013) High-temperature infrared properties of forsterite.
623 Phys Chem Miner 40:287–298. https://doi.org/10.1007/s00269-013-0570-z

624 Edwards CS, Christensen PR (2013) Microscopic emission and reflectance thermal infrared spectroscopy:
625 instrumentation for quantitative in situ mineralogy of complex planetary surfaces. Appl Opt 52:2200.
626 https://doi.org/10.1364/AO.52.002200

article in press

First EC, Mishra I, Gazel E, et al (2024) Potential for observing geological diversity from mid-infrared spectra of rocky exoplanets. Nat Astron 9:370–379. https://doi.org/10.1038/s41550-024-02412-7

Fortin M-A, Gazel E, Williams DB, et al (2024) Lava Worlds Surface Measurements at High Temperatures. Astrophys J Lett 974:L7. https://doi.org/10.3847/2041-8213/ad7d89

Giulietti N, Cosoli G, Napolitano R, et al (2025) Spectral emissivity measurement for high-temperature applications: a systematic review. Acta IMEKO 14:1–17. https://doi.org/10.21014/actaimeko.v14i1.1846

Glaze L, Francis PW, Rothery DA (1989) Measuring thermal budgets of active volcanoes by satellite remote sensing. Nature 338:144–146. https://doi.org/10.1038/338144a0

Hardgrove C, Rogers AD (2013) Thermal infrared and Raman microspectroscopy of moganite-bearing rocks. Am Mineral 98:78–84. https://doi.org/10.2138/am.2013.4152

Helbert J, Maturilli A, Dyar MD, et al (2017) First set of laboratory Venus analog spectra for all atmospheric windows. 2

Howell JR, Mengüç MP, Daun K, Siegel R (2020) Thermal Radiation Heat Transfer, 7th edn. CRC Press, Seventh edition. | Boca Raton : CRC Press, 2021. | Revised edition of: Thermal radiation heat transfer / John R. Howell, M. Pinar Mengüç, Robert Siegel. Sixth edition. 2015.

Koirala LR (2023) A Review on Measurement of Spectral Directional Emissivity of Microstructured Surfaces in Infrared Wavelength Range. KEC J Sci Eng 7:1–9. https://doi.org/10.3126/kjse.v7i1.60510

Kokaly RF, Clark NR, Swayze G, et al (2017) USGS Spectral Library Version 7

Krapez J-C (2025) Multiwavelength thermometry without a priori emissivity information: from promise to disillusionment

Lachance RL (2000) Non-linearity correction of FTIR instruments. ABB Bomem, Quebec city, p 26

Li H, Andujar J, Slodczyk A, et al (2021) Spectral Emissivity of Phonolite Lava at High Temperature. IEEE Trans Geosci Remote Sens 1–15. https://doi.org/10.1109/TGRS.2021.3104657

Lombardo V, Buongiorno MF (2006) Lava flow thermal analysis using three infrared bands of remote-sensing imagery: A study case from Mount Etna 2001 eruption. Remote Sens Environ 101:141–149. https://doi.org/10.1016/j.rse.2005.12.008

Maturilli A, Helbert J (2014) Characterization, testing, calibration, and validation of the Berlin emissivity database. J Appl Remote Sens 8:084985. https://doi.org/10.1117/1.JRS.8.084985

Meerdink SK, Hook SJ, Roberts DA, Abbott EA (2019) The ECOSTRESS spectral library version 1.0. Remote Sens Environ 230:111196. https://doi.org/10.1016/j.rse.2019.05.015

Nádudvari Á, Abramowicz A, Maniscalco R, Viccaro M (2020) The Estimation of Lava Flow Temperatures Using Landsat Night-Time Images: Case Studies from Eruptions of Mt. Etna and Stromboli (Sicily, Italy), Kīlauea (Hawaii Island), and Eyjafjallajökull and Holuhraun (Iceland). Remote Sens 12:2537. https://doi.org/10.3390/rs12162537

Paragas K, Knutson HA, Hu R, et al (2025) A New Spectral Library for Modeling the Surfaces of Hot, Rocky Exoplanets. Astrophys J 981:130. https://doi.org/10.3847/1538-4357/ada9eb

article in press

665 Petrov VA, Reznik VY (1972) Measurement of the emissivity of quartz glass. High Temp - High Press
666 4:687–693

667 Pieters M, Hiroi T (2004) RELAB (reflectance experiment laboratory): a NASA multiuser spectroscopy.

668 Ren D, Tan H, Xuan Y, et al (2016) Apparatus for Measuring Spectral Emissivity of Solid Materials at
669 Elevated Temperatures. Int J Thermophys 37:51. https://doi.org/10.1007/s10765-016-2058-9

670 Rogic N, Bilotta G, Ganci G, et al (2022) The Impact of Dynamic Emissivity–Temperature Trends on
671 Spaceborne Data: Applications to the 2001 Mount Etna Eruption. Remote Sens 14:1641.
672 https://doi.org/10.3390/rs14071641

673 Rogic N, Cappello A, Ferrucci F (2019) Role of Emissivity in Lava Flow 'Distance-to-Run' Estimates from
674 Satellite-Based Volcano Monitoring. Remote Sens 11:662. https://doi.org/10.3390/rs11060662

675 Rozenbaum O, De Sousa Meneses D, Echegut P (2009) Texture and Porosity Effects on the Thermal
676 Radiative Behavior of Alumina Ceramics. Int J Thermophys 30:580–590.
677 https://doi.org/10.1007/s10765-008-0510-1

678 Rozenbaum O, Meneses DDS, Auger Y, et al (1999) A spectroscopic method to measure the spectral
679 emissivity of semi-transparent materials up to high temperature. Rev Sci Instrum 70:4020–4025.
680 https://doi.org/10.1063/1.1150028

681 Salisbury JW, D'Aria DM (1992) Emissivity of terrestrial materials in the 8–14 μm atmospheric window.
682 Remote Sens Environ 42:83–106. https://doi.org/10.1016/0034-4257(92)90092-X

683 Shan S, Chen C, Loutzenhiser PG, et al (2020) Spectral emittance measurements of micro/nanostructures in
684 energy conversion: a review. Front Energy 14:482–509. https://doi.org/10.1007/s11708-020-0693-0

685 Stefan J (1879) Über die Beziehung zwischen der Wärmestrahlung und der Temperatur. Sitzungsberichte
686 Math-Naturwissenschaftlichen Cl Kais Akad Wiss 391–428

687 Storz J, Reitze MP, Stojic AN, et al (2024) Micro-FTIR reflectance spectroscopy of Ryugu, CI chondrites
688 and volatile-rich clasts – Comparing spectral features in the Mid-IR (2.5–16.5 μm) region. Icarus
689 420:116189. https://doi.org/10.1016/j.icarus.2024.116189

690 Thompson JO, Ramsey MS (2021) The influence of variable emissivity on lava flow propagation modeling.
691 Bull Volcanol 83:41. https://doi.org/10.1007/s00445-021-01462-3

692 Thompson JO, Ramsey MS (2020) Uncertainty Analysis of Remotely-Acquired Thermal Infrared Data to
693 Extract the Thermal Properties of Active Lava Surfaces. Remote Sens 12:193.
694 https://doi.org/10.3390/rs12010193

695 Thompson JO, Williams DB, Lee RJ, Ramsey MS (2021) Quantitative Thermal Emission Spectroscopy at
696 High Temperatures: A Laboratory Approach for Measurement and Calibration. J Geophys Res Solid
697 Earth 126:. https://doi.org/10.1029/2021JB022157

698 Thompson MA, Sossi PA, Bower DJ, et al (2025) Water solubility in silicate melts: The effects of melt
699 composition under reducing conditions and implications for nebular ingassing on rocky planets.
700 Chem Geol 695:123048. https://doi.org/10.1016/j.chemgeo.2025.123048

701 Wang F, Cheng L, Mei H, et al (2014) Effect of Surface Microstructures on the Infrared Emissivity of
702 Graphite. Int J Thermophys 35:62–75. https://doi.org/10.1007/s10765-013-1533-9

703 Watanabe H, Ishii J, Wakabayashi H, et al (2014) Spectral Emissivity Measurements. In: Experimental
704 Methods in the Physical Sciences. Elsevier, pp 333–366

705 Weber I, Reitze MP, Morlok A, et al (2023) Mid-IR spectral properties of different surfaces of silicate
706 mixtures before and after excimer laser irradiation. Icarus 404:115683.
707 https://doi.org/10.1016/j.icarus.2023.115683

708 Wenrich ML, Christensen PR (1996) Optical constants of minerals derived from emission spectroscopy:
709 Application to quartz. J Geophys Res Solid Earth 101:15921–15931.
710 https://doi.org/10.1029/96JB01153

711 Xiao Y, Wan C, Shahsafi A, et al (2020) Precision Measurements of Temperature-Dependent and
712 Nonequilibrium Thermal Emitters. Laser Photonics Rev 14:1900443.
713 https://doi.org/10.1002/lpor.201900443

714 Yao C, Mei H, Xiao Y, et al (2022) Correcting thermal-emission-induced detector saturation in infrared
715 spectroscopy. Opt Express 30:38458. https://doi.org/10.1364/OE.466102

716 Ye C, Rucks MJ, Arnold JA, Glotch TD (2019) Mid-Infrared Optical Constants of Labradorite, a Triclinic
717 Plagioclase Mineral. Earth Space Sci 6:2410–2422. https://doi.org/10.1029/2019EA000915

718